

Provided by the author(s) and University of Galway in accordance with publisher policies. Please cite the published version when available.

Title	In-situ SEM study of fatigue micro-crack initiation and propagation behavior in pre-corroded AA7075-T7651
Author(s)	Song, Haipeng; Liu, Changchun; Zhang, Hao; Du, Juan; Yang, Xudong; Leen, Sean B.
Publication Date	2020-04-18
Publication Information	Song, Haipeng, Liu, Changchun, Zhang, Hao, Du, Juan, Yang, Xudong, & Leen, Sean B. (2020). In-situ SEM study of fatigue micro-crack initiation and propagation behavior in pre-corroded AA7075-T7651. International Journal of Fatigue, 137, 105655. doi: <a href="https://doi.org/10.1016/j.ijfatigue.2020.105655">https://doi.org/10.1016/j.ijfatigue.2020.105655</a>
Publisher	Elsevier
Link to publisher's version	<a href="https://doi.org/10.1016/j.ijfatigue.2020.105655">https://doi.org/10.1016/j.ijfatigue.2020.105655</a>
Item record	<a href="http://hdl.handle.net/10379/16147">http://hdl.handle.net/10379/16147</a>
DOI	<a href="http://dx.doi.org/10.1016/j.ijfatigue.2020.105655">http://dx.doi.org/10.1016/j.ijfatigue.2020.105655</a>

Downloaded 2024-04-10T07:12:35Z

Some rights reserved. For more information, please see the item record link above.



# ***In-situ* SEM study of fatigue micro-crack initiation and propagation behavior in pre-corroded AA7075-T7651**

Haipeng Song<sup>a,\*</sup>, Changchun Liu<sup>a</sup>, Hao Zhang<sup>b</sup>, Juan Du<sup>a</sup>, Xudong Yang<sup>a</sup>, Sean B. Leen<sup>c</sup>

<sup>a</sup> *Sino-European Institute of Aviation Engineering, Civil Aviation University of China, China*

<sup>b</sup> *College of Mechanical Engineering, Yangzhou University, China*

<sup>c</sup> *Mechanical Engineering, College of Engineering and Informatics, NUI Galway, Ireland*

## **Abstract (Limit 100 words)**

Fatigue micro-cracking behavior in pre-corroded AA7075-T7651 is analyzed by *in-situ* scanning electron microscopy (SEM) observation and SEM-based fractography. The experimental results show that (i) fatigue micro-cracks nucleated mainly from inclusions at the specimen notch and from corrosion pits on the specimen surface, (ii) pre-corrosion severity degree and maximum stress level significantly affected the extent and time of micro-crack initiation. Corrosion pits are shown to play a crucial role in fatigue micro-crack propagation, due to crack deflection (light corrosion) and crack coalescence (severe corrosion). The growth rate of minor cracks was suppressed by pre-dominant rapid propagation of the main crack.

**Keywords:** Aluminum alloy; Corrosion pit; Fatigue; Micro-crack; *In-situ* SEM observation

---

\* Corresponding author.

E-mail address: hpsong@cauc.edu.cn (Haipeng Song).

## 1. Introduction

Localized corrosion such as corrosion pits are known to promote fatigue failure of aluminum alloy (AA) components in aircraft with increasing service time, which is considered to be one of the most serious issue in aging aircraft [1, 2]. A thorough understanding of the localized corrosion-enhanced cracking behavior in aeronautic aluminum alloy is required to improve the airframe structural integrity management methodology for flight safety and economic maintenance.

On one hand, many studies have addressed this by experimentally observing the crack initiation and propagation in aluminum alloy with localized corrosion [3-8]. Fractographic analysis via scanning electron microscopy (SEM) observation showed that corrosion pits caused accelerated multiple-site cracks initiation in AA2024-T3 [9]. Using the same method, it was found that a fatigue crack initiated from corrosion pits clustered as a semi-elliptical surface micro-notch, rather than the deepest corrosion pit in AA7075-T6511 [8]. To capture more detailed crack initiation characteristics, interrupted tests after pre-defined numbers of fatigue cycles were conducted on corroded AA2024-T3 and then directly tensile tested to fracture; fractographic observations indicated that crack initiation was essentially immediate upon application of the cyclic loading [10]. It has also been observed by microscopy that the pit-to-crack transition of AA7075-T651 depends on the topographic and microscopic features of corrosion pits, as well as the applied fatigue stress level [11]. Crack initiation and propagation in pre-corroded AA7050-T7651 were observed by digital image correlation; results showed that the propagation and coalescence of cracks originated from localized corrosion resulted in the final failure [12]. Values of  $da/dN$  in AA7050-T7451, determined by microscopy of programmed load-induced crack surface markers, were found to be independent of the corrosion damage morphology [5]. Optical microscopy monitoring of pre-corroded AA7075-T6 specimen surfaces revealed that the crack growth rates in salt water were 2 to 12 times larger than corresponding rates in laboratory air [13]. On the other hand, some modelling work corresponding to experimental observation has also been conducted to analyze the crack initiation and propagation from localized corrosion in aluminum alloys [14-17]. The stress distribution in a corrosion pit was numerically analyzed by the finite element method in which the actual pit was idealized as a semi-elliptical shape [18]. A continuum damage mechanics model was used to predict the corrosion-fatigue crack initiation life of AA2024-T3, assuming that one dominant corrosion pit grows to a critical depth and transitions into a fatigue crack, even though several corrosion pits may be present. Based on linear elastic fracture mechanics, the fatigue crack growth in pre-corroded AA7075-T6511 under constant and variable amplitude fatigue loading was simulated using a corrosion-modified equivalent initial flaw size, which was in agreement with experimental

results [19]. A cumulative crack growth methodology based on the Willenborg-Chang rule was presented to successfully evaluate the residual life of aluminum alloy under corrosion-fatigue conditions [20].

However, the evolution characteristics of micro-crack initiation and propagation during fatigue, especially associated with corrosion damage morphology and material micro-structure, remains unclear. Previous work experimentally investigated the fatigue cracking behavior mainly based on fractography; the direct *in-situ* observation of fatigue micro-crack initiation and propagation in pre-corroded typical aeronautic aluminum alloy (such as 2xxx and 7xxx), which would be helpful for understanding the material failure mechanism, has rarely been reported. Previous studies have demonstrated that *in-situ* testing, with scanning electron microscopy (SEM), is an effective way to investigate micro-crack initiation and propagation in metals [21, 22]. In this paper, constant amplitude fatigue tests are carried out on pre-corroded AA7075-T7651 under *in-situ* SEM observation. The fatigue micro-crack initiation and propagation behavior associated with different levels of prior corrosion damage and maximum fatigue stress are analyzed and discussed via the combined analysis of *in-situ* SEM observation and SEM-based fractography.

## 2. Experiment

The material used in this study is AA7075-T7651 (Si-0.4 Ti-0.2 Cr-0.18-0.28 Fe-0.5 Mg-2.1-2.9 Cu-1.2-2.0 Mn-0.3 Zn-5.1-6.1 Al; wt%). The monotonic tensile yield strength is 486.8 MPa and the ultimate tensile strength is 520.2 MPa. Dog-bone shaped specimens with a single-edge notch were cut for testing, as shown in Fig. 1 (a). The material metallographic structure of the L-S plane of AA7075-T7651 is shown in Fig. 1 (b). Two groups of specimens were exposed to exfoliation corrosion (EXCO) solution according to ASTM G34-01 [23] for 0.5 and 1 hour respectively, to produce different levels of initial corrosion damage. Considering that just one surface of the specimen could be observed during the *in-situ* SEM testing, here only the front surface (L-S plane) for each sample was exposed to EXCO during the corrosion process; while other surfaces were masked by the adhesive tape. The corrosive solution consisted of the following chemicals diluted in 1L distilled water: sodium chloride (234g NaCl), potassium nitrate (50g KNO<sub>3</sub>) and nitric acid (6.3mL HNO<sub>3</sub>). SEM is combined with the servo-hydraulic fatigue machine (SHIMADZU SEM-SERVO), as shown in Fig. 2 (a), to facilitate *in-situ* SEM fatigue tests on the specimens at room temperature. Sine wave loading with a frequency of 10 Hz was used, as shown in Fig. 2 (b). Two groups of maximum applied tensile stresses were chosen as 333 MPa and 389 MPa, corresponding to about 65% and 75% of the ultimate tensile strength, to analyze the fatigue micro-cracking behavior in different fatigue maximum stress conditions. It should be noted that in some special cases, such as aircraft landing, taxiing, tactical operation, and extreme weather, aluminum alloy aircraft structures can

experience high cyclic loads, potentially leading to premature fatigue damage and failure. Therefore, two relatively high stress levels were chosen in this work. The stress ratio (R) was set as 0.1 for all cases. In each test, the specimen surface at specified numbers of fatigue cycles were observed and captured by SEM.

### 3. Results and discussion

#### 3.1. Fatigue lives in different loading conditions

The fatigue lives of specimens in different experimental conditions are shown in Fig. 3. It can be seen that pre-corrosion damage and fatigue maximum stress have detrimental effects on fatigue performance of AA7075-T7651. For example, at the stress level of  $\sigma_{max} = 333$  MPa and 389 MPa, the fatigue life is reduced by about 21.6% and 24.7%, respectively, when the corrosion exposure increased from 0.5 to 1 hour. For the 1-hour pre-corrosion case, the fatigue life reduced significantly by about 38.5% when the fatigue maximum stress increased from 333 to 389 MPa. The significant corrosion-induced degradation in fatigue life observed in this work is in agreement with previous reported work [24].

#### 3.2. Micro-crack initiation and propagation

The details of fatigue micro-crack initiation and propagation during the present fatigue tests were further analyzed by *in-situ* SEM observation. Fig. 4 showed typical results of the specimen with a corrosion time of 0.5 hour, at the stress level of  $\sigma_{max} = 333$  MPa. A few small corrosion pits were observed on the specimen surface before loading, as shown in Fig. 4 (a). To quantitatively characterize the extent of corrosion on the specimen, pit density is represented by the number of identified corrosion pits near the specimen notch, and the size of pits is represented by a characteristic dimension,  $d$ , of the corrosion pits (such as length of major axis for elliptical corrosion pits). Here, only corrosion pits with characteristic sizes of  $d > 5\mu m$  were considered. The results showed that the number and typical characteristic size of corrosion pits are  $n \approx 3$  and  $d \approx 6\mu m$ , respectively. As fatigue cycles increased to 1,257 cycles, one micro-crack ( $I_1$ ) was found to nucleate at the notch root and another micro-crack ( $I_2$ ) initiated at a corrosion pit on the surface, as shown in Fig. 4 (b) (marked by the white arrow). After that, micro-crack  $I_1$  continued to propagate non-linearly with increasing cycles, while micro-crack  $I_2$  did not propagate, as shown in Fig. 4 (c) and the enlarged view of Fig. 4 (d). Noting that, since micro-crack  $I_1$  is located near the notch root, with a local stress concentration, the driving force of crack propagation (effective stress intensity factor range) for micro-crack  $I_1$  is larger than for micro-crack  $I_2$ , which is located on the specimen surface. With preferential propagation of micro-crack  $I_1$ , the stress field near the tip of micro-crack  $I_2$  is relaxed, to some extent, leading to reduced driving force of crack propagation for micro-crack  $I_2$ . At 4,408

fatigue cycles, as shown in Fig. 4 (e) and its enlarged view of Fig. 4 (f), micro-crack I<sub>1</sub> propagated further across the grain boundary and evolved to be a main crack. It was noted that there was a corrosion pit A located near the tip of main crack I<sub>1</sub>. Under fatigue loading, main crack I<sub>1</sub> changed from the original propagation direction and crossed the corrosion pit, as shown in Fig. 4 (g) and its enlarged view Fig. 4 (h), which demonstrates a detrimental effect on cracking path of a stress concentration due to a corrosion pit located near a crack tip, e.g. according to the maximum energy release rate theory in fracture mechanics. It is also noted that, the typical corrosion pit are relatively small ( $d \approx 6\mu m$ ) here, so that the effect on crack tip stress fields is negligible for pit away from the crack tip. Finally, the quick propagation of main crack I<sub>1</sub> resulted in final failure.

Fig. 5 illustrates the fatigue failure process of the specimen with a corrosion time of 0.5 hour, at the stress level of  $\sigma_{max} = 389$  MPa. Similarly, a few ( $n \approx 2$ ) small corrosion pits ( $d \approx 8\mu m$ ) were observed on the specimen surface, as shown in Fig. 5 (a). At 1,006 fatigue cycles, a micro-crack II<sub>1</sub> firstly initiated in the notch region but away from the notch root, as shown in Fig. 5 (b). As the cycles increased to 1,507, another micro-crack II<sub>2</sub> also initiated near the notch root, as shown in Fig. 5 (c) and its enlarged view Fig. 5 (d). It is also noted that some micro-cracks nucleated at corrosion pits, as shown in Fig. 5 (d). With further cycles, micro-crack II<sub>2</sub> further propagated and evolved into a main crack, as shown in Fig. 5 (e), while micro-crack II<sub>1</sub> (although initiated earlier than micro-crack II<sub>2</sub>), and other micro-cracks nucleated at corrosion pits, did not further grow. This phenomenon can be explained by the decrease in crack growth driving force due to stress release caused by preferential propagation of the main crack, similar to the description above for the stress level of  $\sigma_{max} = 333$  MPa. After 3,353 cycles, a crack branch phenomenon, including both transgranular and intergranular cracking behavior was observed, as shown in Fig. 5 (g) and its enlarged view Fig. 5 (h). Finally, main crack II<sub>2</sub> propagated quickly along the primary crack branch and caused final fracture.

Fig. 6 shows the micro-crack initiation and propagation to failure in the specimen with a corrosion time of 1 hour, at the stress level of  $\sigma_{max} = 333$  MPa. A cluster of corrosion pits was observed on the specimen surface, as shown in Fig. 6 (a); it can be seen that the number ( $n \approx 9$ ) and sizes ( $d \approx 20\mu m$ ) of corrosion pits are obviously larger than for the 0.5 hour test. A micro-crack III<sub>1</sub> initiated at the specimen notch after 1,002 cycles, remote from the notch root, as shown in Fig. 6 (b). Meanwhile, some micro-cracks nucleated at the cluster of corrosion pits, such as micro-crack III<sub>2</sub>. Compared to the 0.5 hour specimen, more significant corrosion damage is induced in this specimen with increased micro-crack initiation. As fatigue cycles increased to 3,006 cycles, it can be seen that another micro-crack III<sub>3</sub> also initiated at the specimen notch, relatively near to the notch root, as shown in Fig. 6 (c). These micro-cracks at the cluster of corrosion pits propagated further, simultaneously, and coalesced

with adjacent micro-cracks, such as micro-crack III<sub>4</sub>. The growth and coalescence of micro-crack III<sub>3</sub> and micro-crack III<sub>4</sub> eventually evolved into a main crack, as shown in Fig. 6 (e) and the enlarged view in Fig. 6 (f). With increasing fatigue cycles, the main crack quickly propagated in a zig-zag manner with significant deflection, due to the coalescence with micro-cracks originated from other corrosion pits, as shown in Fig. 6 (g); this demonstrates the significant effect of pre-existing localized corrosion on micro-crack propagation. In the case of 0.5 h corrosion, as described above, only the corrosion pits located near the crack tip affected the cracking path. In contrast, here more aggravated pre-existing corrosion damage promoted increased micro-crack initiation. These multiple micro-cracks coalesced with adjacent ones and evolved into larger cracks. Such larger cracks caused local stress concentrations covering a larger volume of material, further affecting the path of the main crack even if they were not near the main crack, due to multiple crack coalescence. Finally, Fig. 6 (h) shows the final failure results due to propagation of the main crack.

Fig. 7 shows the evolution of micro-crack nucleation and propagation in the specimen with corrosion time of 1 hour, at a stress level of  $\sigma_{\max} = 389$  MPa. Fig. 7 (a) shows corrosion pits of different sizes, labelled C, D and E, with largest pit  $d \approx 100\mu m$  located on a pan-caked grain structure or on the grain boundary. Under fatigue loading, numerous micro-cracks nucleate at different corrosion pits and also in the notch region, as shown in Fig. 7 (b) and (c). Micro-crack IV<sub>1</sub>, which initiated from the notch, is found to propagate at an angle of about  $45^\circ$  to the loading direction and coalesce with corrosion pit C after 515 fatigue cycles, as shown in Fig. 7 (b). After 1,006 fatigue cycles, another micro-crack, labelled IV<sub>2</sub>, also nucleates near the notch root, as shown in Fig. 7 (c), and propagates towards corrosion pit D after 1,502 loading cycles (see Fig. 7 (d) and (e)). Micro-crack IV<sub>2</sub> was found to grow quickly under fatigue loading and successively traverse corrosion pit D and E, while other micro-cracks did not propagate, as shown in Fig. 7 (g) and (h). It is interesting to see that, although micro-crack IV<sub>1</sub> formed earlier, micro-crack IV<sub>2</sub> forms the main crack that leads to final failure after 2,646 cycles.

### 3.3. Fracture morphology analysis

Post-failure fracture morphology analysis for the different loading conditions was conducted out to comprehensively characterize the micro-crack initiation and propagation behavior. Fig. 8 shows the fracture morphology for a corrosion time of 0.5 hour, with stress level of  $\sigma_{\max} = 333$  MPa, corresponding to the *in-situ* SEM observation shown in Fig. 4. Fig. 8 (a) shows that the fracture surface consists of (i) a fatigue crack initiation region, (ii) a fatigue crack propagation region and (iii) a transient fracture region. Multiple crack initiation sites were observed in the notch, as shown in the enlarged views of Figs. 8 (b) and (c). A corrosion pit was found to cause initiation of a micro-crack at the corroded (*in-situ* observation) surface shown in Fig. 8 (c),

corresponding to corrosion pit A in Fig. 4 (f). The propagation and coalescence of adjacent micro-cracks formed a ridge, as shown in Fig. 8 (c). Also, quasi-cleavage fracture features are also observed in the fracture morphology, demonstrating hydrogen embrittlement, due to pre-corrosion. Fig. 9 shows the fracture morphology for a corrosion time of 0.5 hour, stress level  $\sigma_{max} = 389$  MPa, corresponding to the *in-situ* SEM observation of Fig. 5. It is obvious that more than one fatigue crack initiation site can be observed in Fig. 9 (a) and the enlarged views of Figs. 9 (b) and (c). An inclusion particle located in the notch was identified as a contributory factor to fatigue crack nucleation, as shown in Fig. 9 (b). Quasi-cleavage fracture features and fatigue striations are also observed in Figs. 9 (c) and (d).

Fig. 10 illustrates the fracture morphology for a corrosion time of 1 hour and stress level  $\sigma_{max} = 333$  MPa, corresponding to the *in-situ* SEM observation of Fig. 6. Again, multiple sites of crack initiation are observed in the notch (Figs. 10 (a), (b) and (c)). From the enlarged view, it can be seen that the main crack initiated at an inclusion located in the notch. A corrosion pit was found to cause micro-crack initiation at the corroded surface, as shown in Fig. 10 (c) and the enlarged view Fig. 10 (d); this corresponds to corrosion pit B of Figs. 6 (e) and (f). The corrosion pit is larger than for the 0.5 hour case shown in Fig. 8 (c). Ridges were also formed due to the propagation and coalescence of adjacent micro-cracks (Fig. 10 (c) and (d)). The fracture surface consists of other features such as dimples and quasi-cleavage fracture, as shown in Figs. 10 (a) and (d). Fig. 11 showed the fracture morphology for 1 hour corrosion time and  $\sigma_{max} = 389$  MPa, for *in-situ* SEM observation of Fig. 7. Multiple fatigue crack initiation sites were again observed in Fig. 11 (a), (b) and (c). From the enlarged view shown in Fig. 11 (b), it was found that a corrosion pit located at the corroded surface promoted crack initiation and the resulting micro-crack nucleated from the notch coalesced with a micro-crack initiated from corrosion pit D to create a ridge. The ridge was also found to coalesce with adjacent micro-cracks located in the notch (Fig. 11 (c)). The propagation path of the main crack across the corrosion pit on the specimen corroded surface as shown in Fig. 11 (d).

### 3.4. Discussion of failure process

Multiple micro-cracks were observed to originate from inclusions located in the notch (Fig. 10 (b)), and from corrosion pits on the specimen surface (Fig. 10 (d)). For a corrosion time of 0.5 hour, corrosion pits on the surface were fewer, smaller ( $d < 10\mu m$ ), and relatively isolated, giving reduced micro-crack initiation and absence of crack coalescence, as shown in Fig. 4. In contrast, for a corrosion time of 1 hour, a cluster of corrosion pits promoted increased micro-crack initiation and coalescence during fatigue, as shown in Fig. 6. Specifically, for the 0.5 hour corrosion case, only about 4 micro-cracks initiated under both stress levels ( $\sigma_{max} =$



333 MPa and  $\sigma_{max} = 389$  MPa); in contrast, for the 1 hour corrosion case, about 10 micro-cracks initiated under both stress levels. This indicates that the number of initiated micro-cracks depends mainly on corrosion damage state, rather than stress level. In addition, at the same stress level, specimens with corrosion of 1 hour took less time to initiate micro-cracks than those of 0.5 hours, as illustrated in Fig. 5 (b) and Fig. 7 (b). Based on the *in-situ* SEM observation and SEM-based fractography, the 1 hour corrosion pits were larger than the 0.5 hour pits, causing larger local stress concentration, hence leading to premature crack initiation.

Experimental observation illustrates that corrosion pits play a crucial role in the propagation of fatigue crack. For pre-corrosion of 0.5 hours, corrosion pits had an influence on propagation direction of the main crack. As shown in Fig. 4 (g), main crack I<sub>1</sub> deviated from the original path and turned towards the corrosion pit. However, due to limited numbers and size of corrosion pits, only pits near the crack-tip affected crack propagation; pits remote from the crack-tip had little effect on crack propagation path. For 1-hour pre-corrosion, micro-cracks were originated from a cluster of corrosion pits and interconnected with adjacent ones into a larger crack, thus affecting the main crack path due to crack coalescence, despite being remote from the main crack-tip, as illustrated in Fig. 6. Experimental observation also showed that the fatigue micro-crack propagation direction and path are affected by material microstructural features, such as grain boundaries, near the crack tip, especially in some regions without obvious corrosion damage, as shown in Fig. 5; both transgranular and intergranular fracture modes were simultaneously observed, reflecting competitive relationships between grain boundary bonding force and grain strength. Generally, when the angle between grain boundary and original crack direction is small, intergranular fracture occurs more easily.

Micro-crack arrest effects were also observed in the multiple crack propagation phenomena, attributed to decrease in driving force of crack propagation due to stress release caused by propagation of other cracks. The first crack initiated did not necessarily lead to final fracture. As shown in Fig. 5, crack II<sub>1</sub> arrested after initiation of main crack II<sub>2</sub>, indicating that propagation of the main crack had an inhibiting effect on secondary crack propagation. The lengths of main and secondary cracks for specimens under different experimental conditions were plotted versus numbers of fatigue cycles in Fig. 12, thus demonstrating that decreased propagation rate or arrest of secondary cracks after main crack initiation.

#### 4. Conclusions

Fatigue micro-crack initiation and propagation in pre-corroded aluminum alloy 7075-T7651 was experimentally analyzed by *in-situ* SEM observation and SEM-based fractography. It was found that:

(1) The degree of severity of pre-corrosion and maximum fatigue stress significantly reduced the fatigue

resistance of AA7075-T7651. In the context of degradation of fatigue life, the combined analysis of *in-situ* SEM observation and SEM-based fractography is an effective method to describe and analyze the spatial-temporal evolution characteristics of fatigue micro-crack initiation and propagation in pre-corroded AA7075-T7651.

(2) Micro-cracks were found to initiate predominantly from inclusions located at the specimen notch and from corrosion pits on the specimen surface; the quantity and rate of crack initiation increased with increasing severity of pre-corrosion.

(3) For specimens with severe corrosion, corrosion pits are the key factor controlling crack propagation path; micro-cracks originating from clusters of corrosion pits became interconnected with adjacent ones to form a larger crack, thus affecting the main crack path via coalescence. For specimens with light corrosion, only corrosion pits near main crack-tip affect crack propagation path.

(4) Both transgranular and intergranular propagation modes were observed, demonstrating the effect of micro-structure on crack propagation in cases with no obvious corrosion damage. In addition, crack arrest phenomena were observed between multiple cracks, whereby (i) the first crack formed does not necessarily become the main crack, and (ii) the main crack has an inhibiting effect on propagation of secondary cracks.

## Acknowledgements

This research was supported by the National Natural Science Foundation of China (NSFC, Grant Nos. 11972364, 11502285 and 51971242), the Science Foundation Ireland (SFI, Grant No. 14/IA/2604) and the Fundamental Research Funds for the Central Universities (FRFCU, Grant No. 3122014H006).

## References

- [1] S.A. Barter, L. Molent, Fatigue cracking from a corrosion pit in an aircraft bulkhead, *Engineering Failure Analysis*, 39 (2014) 155-163.
- [2] L. Molent, Managing airframe fatigue from corrosion pits – A proposal, *Engineering Fracture Mechanics*, 137 (2015) 12-25.
- [3] Y. Chen, J. Zhou, C. Liu, F. Wang, Effect of pre-deformation on the pre-corrosion multiaxial fatigue behaviors of 2024-T4 aluminum alloy, *International Journal of Fatigue*, 108 (2018) 35-46.
- [4] V. Sabelkin, S. Mall, H. Misak, Investigation into Corrosion Pit-to-Fatigue Crack Transition in 7075-T6 Aluminum Alloy, *Journal of Materials Engineering and Performance*, 26 (2017) 2535-2541.
- [5] N.E.C. Co, J.T. Burns, Effects of macro-scale corrosion damage feature on fatigue crack initiation and

- fatigue behavior, *International Journal of Fatigue*, 103 (2017) 234-247.
- [6] H.E. Misak, V.Y. Perel, V. Sabelkin, S. Mall, Biaxial tension–tension fatigue crack growth behavior of 2024-T3 under ambient air and salt water environments, *Engineering Fracture Mechanics*, 118 (2014) 83-97.
- [7] J.T. Burns, S. Kim, R.P. Gangloff, Effect of corrosion severity on fatigue evolution in Al–Zn–Mg–Cu, *Corrosion Science*, 52 (2010) 498-508.
- [8] S. Kim, J.T. Burns, R.P. Gangloff, Fatigue crack formation and growth from localized corrosion in Al–Zn–Mg–Cu, *Engineering Fracture Mechanics*, 76 (2009) 651-667.
- [9] K. van der Walde, J.R. Brockenbrough, B.A. Craig, B.M. Hillberry, Multiple fatigue crack growth in pre-corroded 2024-T3 aluminum, *International Journal of Fatigue*, 27 (2005) 1509-1518.
- [10] K. van der Walde, B.M. Hillberry, Initiation and shape development of corrosion-nucleated fatigue cracking, *International Journal of Fatigue*, 29 (2007) 1269-1281.
- [11] J.T. Burns, J.M. Larsen, R.P. Gangloff, Driving forces for localized corrosion-to-fatigue crack transition in Al–Zn–Mg–Cu, *Fatigue & Fracture of Engineering Materials & Structures*, 34 (2011) 745-773.
- [12] H. Song, Z. Bai, H. Zhang, Y. Niu, S. Leen, Effect of pre - corrosion on damage evolution and crack propagation in aluminum alloy 7050 - T7651, *Fatigue & Fracture of Engineering Materials & Structures*, (2018).
- [13] G. Joshi, S. Mall, Crack Initiation and Growth from Pre-corroded Pits in Aluminum 7075-T6 Under Laboratory Air and Salt Water Environments, *Journal of Materials Engineering and Performance*, 26 (2017) 2293-2304.
- [14] Y.F. Huang, X.B. Ye, B.R. Hu, L.J. Chen, Equivalent crack size model for pre-corrosion fatigue life prediction of aluminum alloy 7075-T6, *International Journal of Fatigue*, 88 (2016) 217-226.
- [15] P. Hu, Q.C. Meng, W.P. Hu, F. Shen, Z.X. Zhan, L.L. Sun, A continuum damage mechanics approach coupled with an improved pit evolution model for the corrosion fatigue of aluminum alloy, *Corrosion Science*, 113 (2016) 78-90.
- [16] W.P. Hu, Q.A. Shen, M. Zhang, Q.C. Meng, X. Zhang, Corrosion-Fatigue Life Prediction for 2024-T62 Aluminum Alloy Using Damage Mechanics-Based Approach, *International Journal of Damage Mechanics*, 21 (2012) 1245-1266.
- [17] M. Cerit, Numerical investigation on torsional stress concentration factor at the semi elliptical corrosion pit, *Corrosion Science*, 67 (2013) 225-232.
- [18] Y. Huang, T. Gang, L. Chen, Interacting Effects Induced by Two Neighboring Pits Considering Relative Position Parameters and Pit Depth, *Materials*, 10 (2017) 398.
- [19] M. McMurtrey, D. Bae, J. Burns, Fracture mechanics modelling of constant and variable amplitude fatigue behaviour of field corroded 7075 - T6511 aluminium, *Fatigue & Fracture of Engineering Materials & Structures*, 40 (2017) 605-622.
- [20] C.Q. Wang, J.J. Xiong, R.A. Shenoi, M.D. Liu, J.Z. Liu, A modified model to depict corrosion fatigue crack growth behavior for evaluating residual lives of aluminum alloys, *International Journal of Fatigue*, 83 (2016) 280-287.
- [21] Z. Wang, W. Wu, G. Qian, L. Sun, X. Li, J.A.F.O. Correia, In-situ SEM investigation on fatigue behaviors of additive manufactured Al-Si10-Mg alloy at elevated temperature, *Engineering Fracture Mechanics*, 214 (2019) 149-163.
- [22] X. Ma, H.-J. Shi, In situ SEM studies of the low cycle fatigue behavior of DZ4 superalloy at elevated temperature: Effect of partial recrystallization, *International Journal of Fatigue*, 61 (2014) 255-263.
- [23] A. Standard, G34-01, Standard Test Method for Exfoliation Corrosion Susceptibility in 2XXX and 7XXX Series Al Alloys, (2001).
- [24] N.E.C. Co, J.T. Burns, Galvanic Corrosion-Induced Fatigue Crack Initiation and Propagation Behavior in AA7050-T7451, *CORROSION*, 72 (2016) 1215-1219.

### Figure Captions

Fig. 1. (a) Schematic diagram of specimen, (b) microstructure of AA7075-T7651 along the L-S direction.

Fig. 2. (a) Experimental apparatus for in-situ SEM fatigue tests, (b) applied fatigue stress waveforms.

Fig. 3. Measured fatigue lives of pre-corroded AA7075-T7651 under different experimental conditions.

Fig. 4. *In-situ* SEM observation of fatigue failure process of specimen with a corrosion time of 0.5 hour, at a

stress level of  $\sigma_{\max} = 333$  MPa; the yellow squares are the field of view of subsequent images.

Fig. 5. *In-situ* SEM observation of fatigue failure process of specimen with a corrosion time of 0.5 hour, at a stress level of  $\sigma_{\max} = 389$  MPa; the yellow squares are the field of view of subsequent images.

Fig. 6. *In-situ* SEM observation of fatigue failure process of specimen with a corrosion time of 1 hour, at a stress level of  $\sigma_{\max} = 333$  MPa; the yellow squares are the field of view of subsequent images.

Fig. 7. *In-situ* SEM observation of fatigue failure process of specimen with a corrosion time of 1 hour, at a stress level of  $\sigma_{\max} = 389$  MPa; the yellow squares are the field of view of subsequent images.

Fig. 8. Fracture morphology of specimen with a corrosion time of 0.5 hour, at a stress level of  $\sigma_{\max} = 333$  MPa, corresponding to the specimen shown in Fig. 4; the yellow squares are the field of view of subsequent images.

Fig. 9. Fracture morphology of specimen with corrosion time of 0.5 hour, at a stress level of  $\sigma_{\max} = 389$  MPa, corresponding to the specimen shown in Fig. 5; the yellow squares are the field of view of subsequent images.

Fig. 10. Fracture morphology of specimen with corrosion time of 1 hour, at a stress level of  $\sigma_{\max} = 333$  MPa, corresponding to the specimen shown in Fig. 6; the yellow squares are the field of view of subsequent images.

Fig. 11. Fracture morphology of specimen with corrosion time of 1 hour, at a stress level of  $\sigma_{\max} = 389$  MPa, corresponding to the specimen shown in Fig. 7; the yellow squares are the field of view of subsequent images.

Fig. 12. Fatigue crack length curves of main crack (denoted by red line) and minor crack (denoted by blue line) versus fatigue cycle for different experimental conditions.

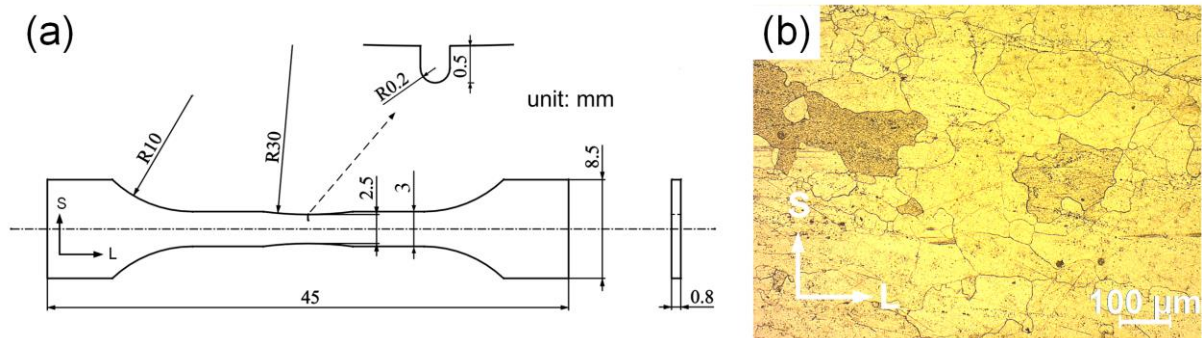


Fig. 1. (a) Schematic diagram of specimen, (b) microstructure of AA7075-T7651 along the L-S direction.

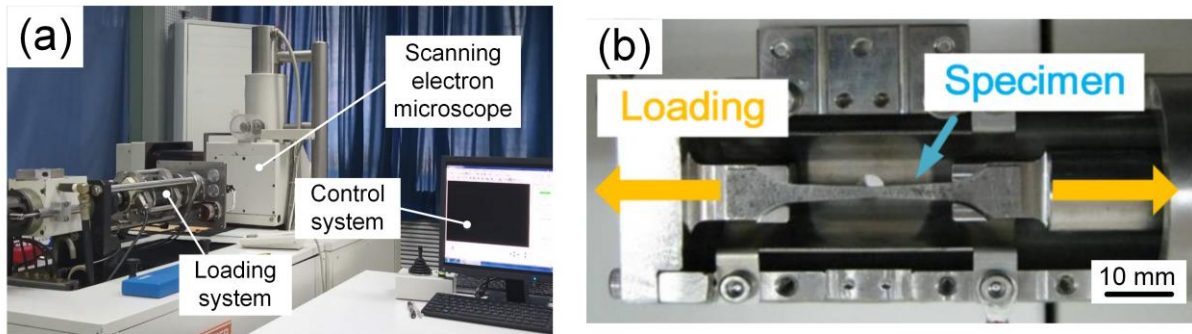


Fig. 2. (a) Experimental apparatus for *in-situ* SEM fatigue tests, (b) applied fatigue stress waveforms.

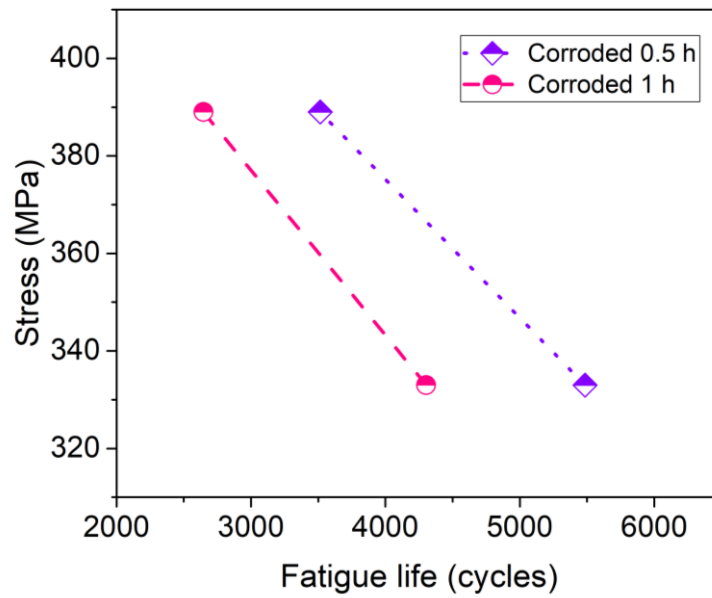


Fig. 3. Measured fatigue lives of pre-corroded AA7075-T7651 under different experimental conditions.



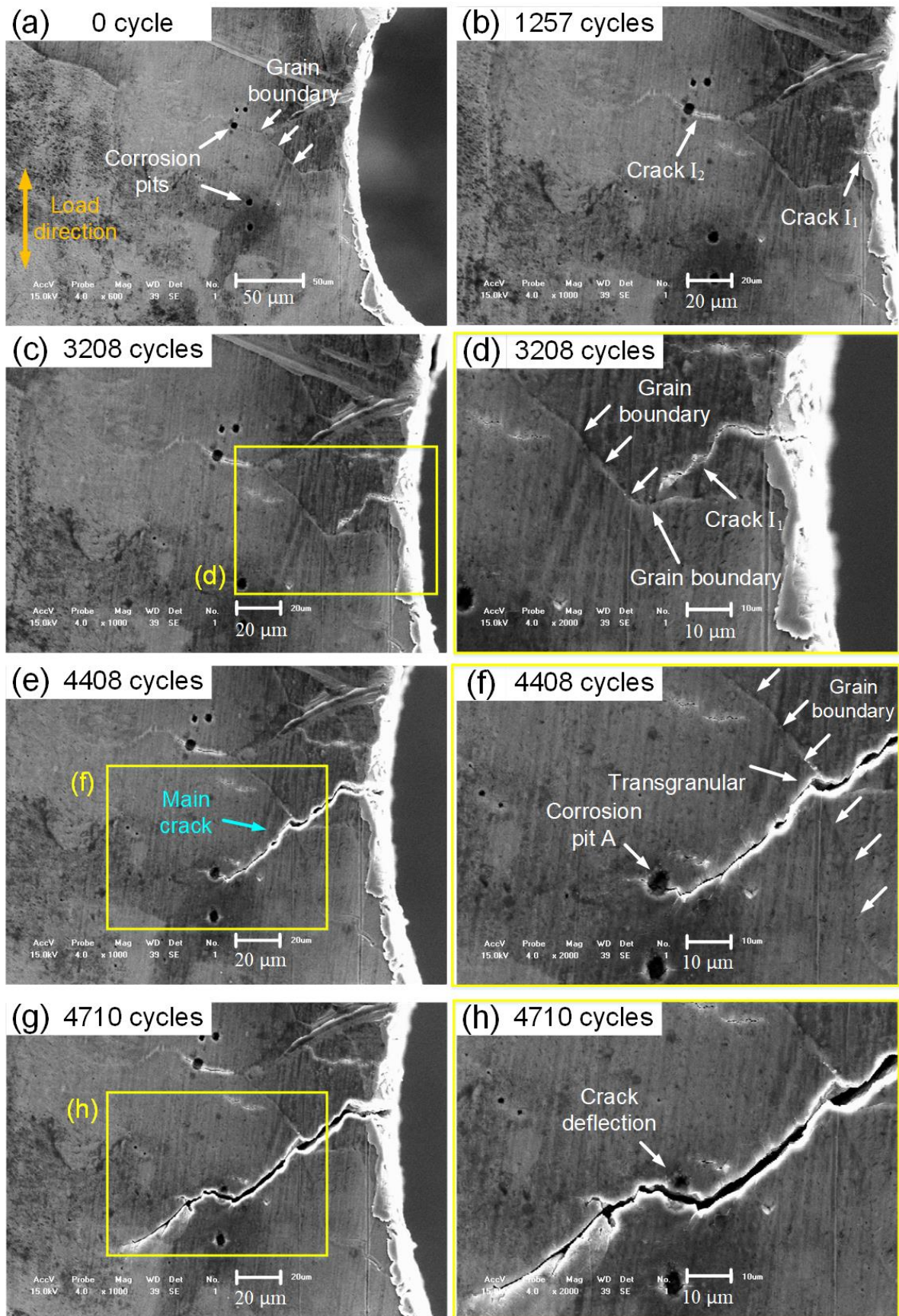


Fig. 4. *In-situ* SEM observation of fatigue failure process of specimen with a corrosion time of 0.5 hour, at a stress level of  $\sigma_{\max} = 333$  MPa; the yellow squares are the field of view of subsequent images.



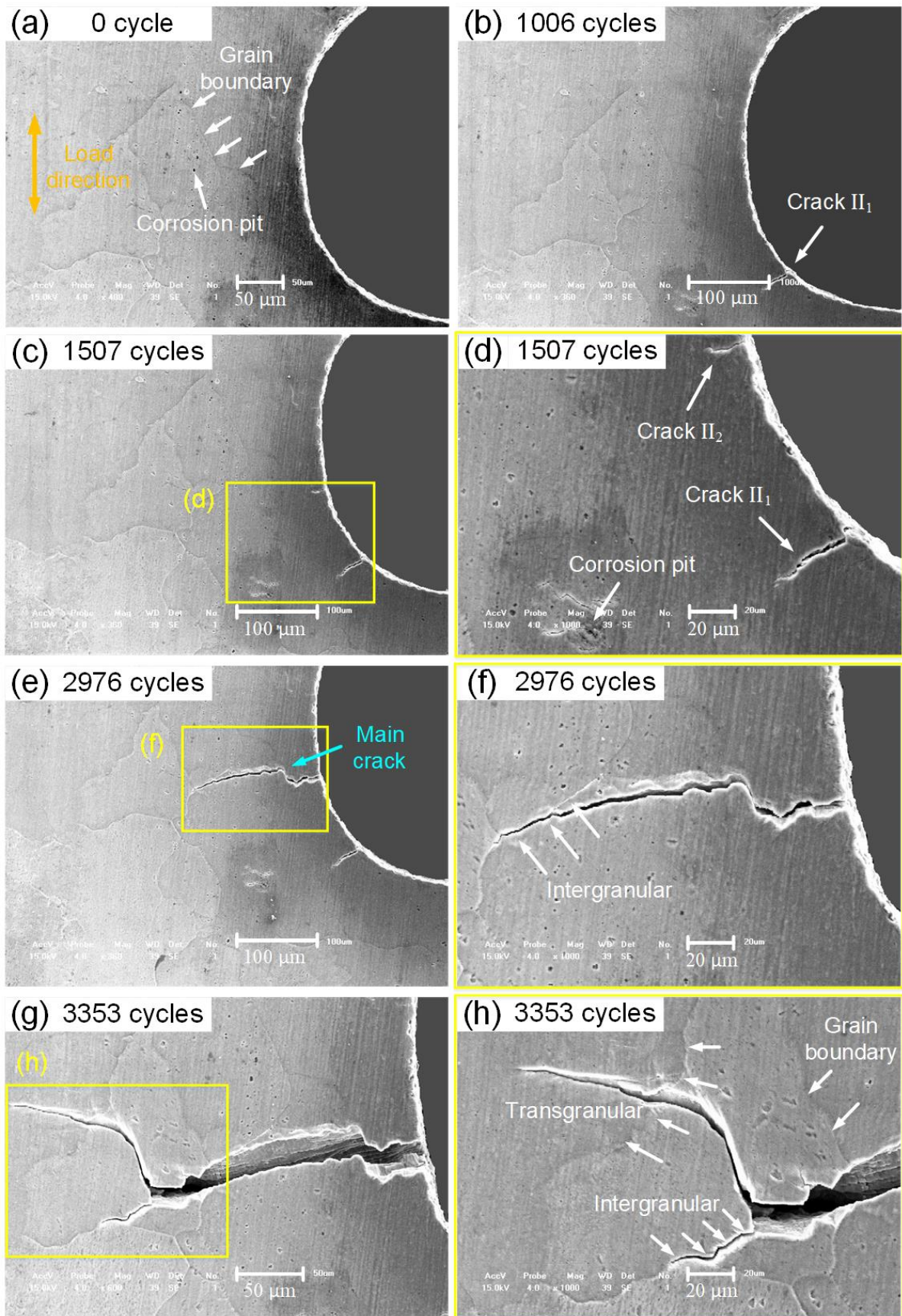


Fig. 5. *In-situ* SEM observation of fatigue failure process of specimen with a corrosion time of 0.5 hour, at a stress level of  $\sigma_{\max} = 389$  MPa; the yellow squares are the field of view of subsequent images.



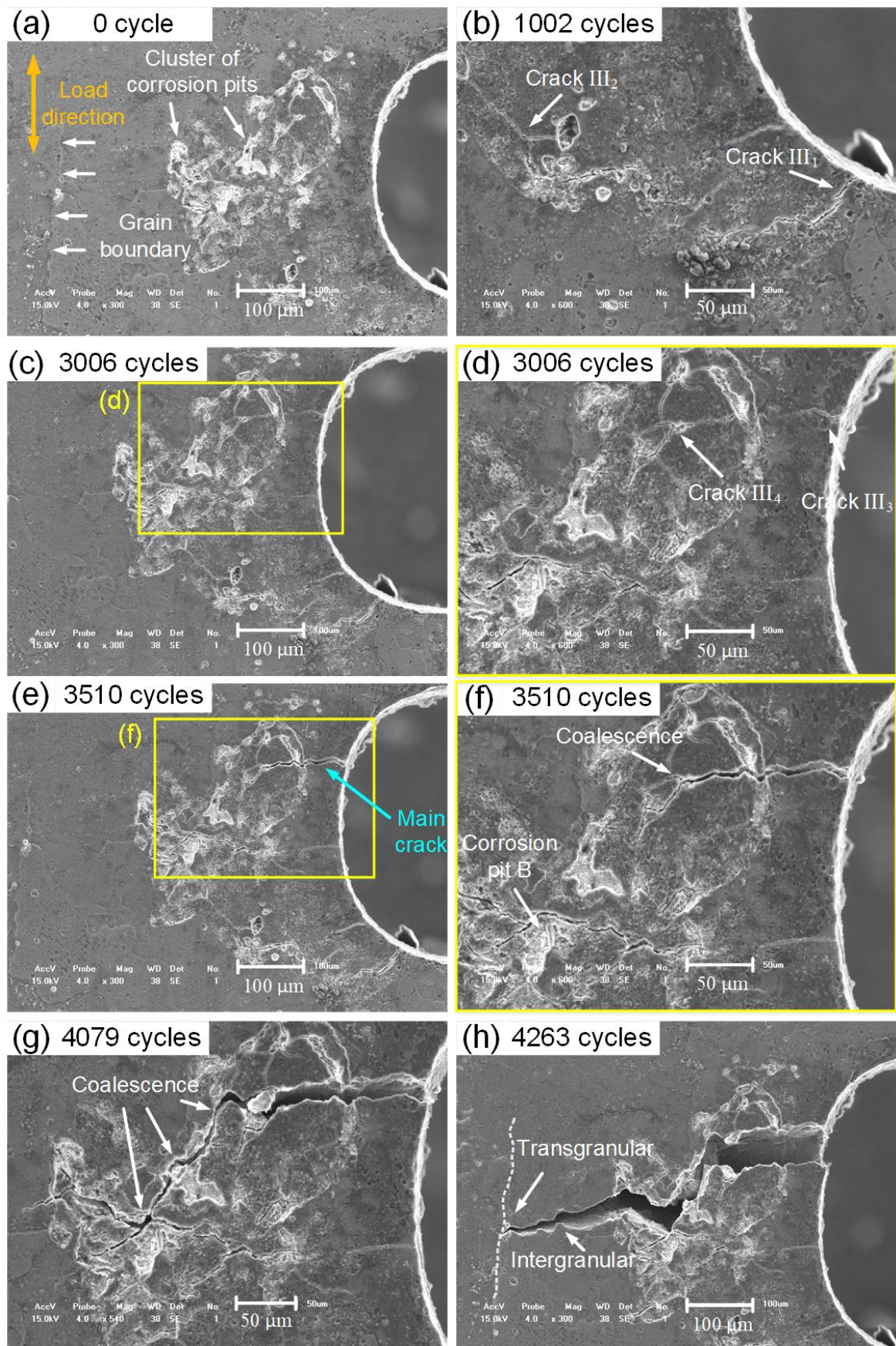


Fig. 6. *In-situ* SEM observation of fatigue failure process of specimen with a corrosion time of 1 hour, at a stress level of  $\sigma_{\max} = 333$  MPa; the yellow squares are the field of view of subsequent images.



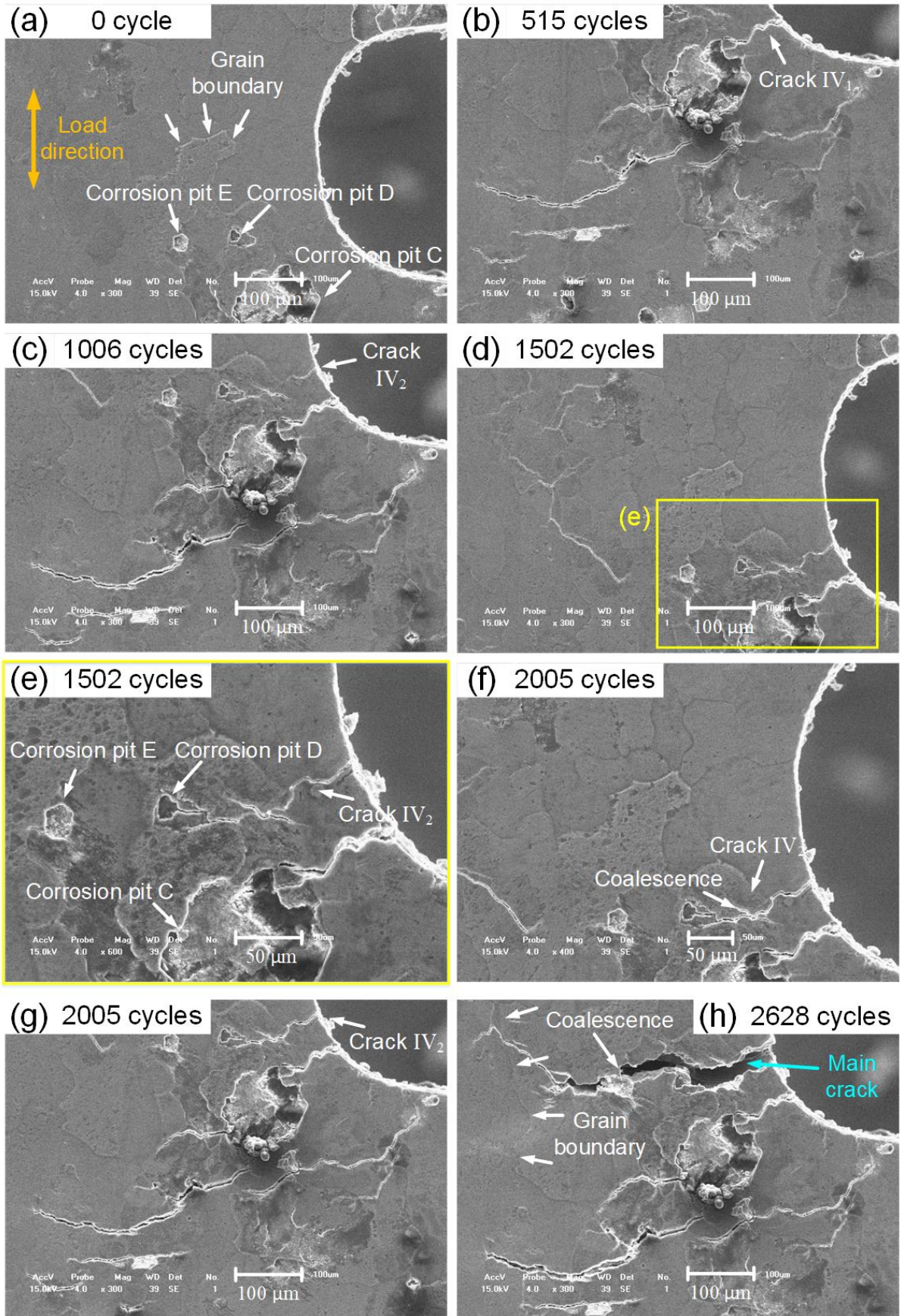


Fig. 7. In-situ SEM observation of fatigue failure process of specimen with a corrosion time of 1 hour, at a stress level of  $\sigma_{\max} = 389$  MPa; the yellow squares are the field of view of subsequent images.

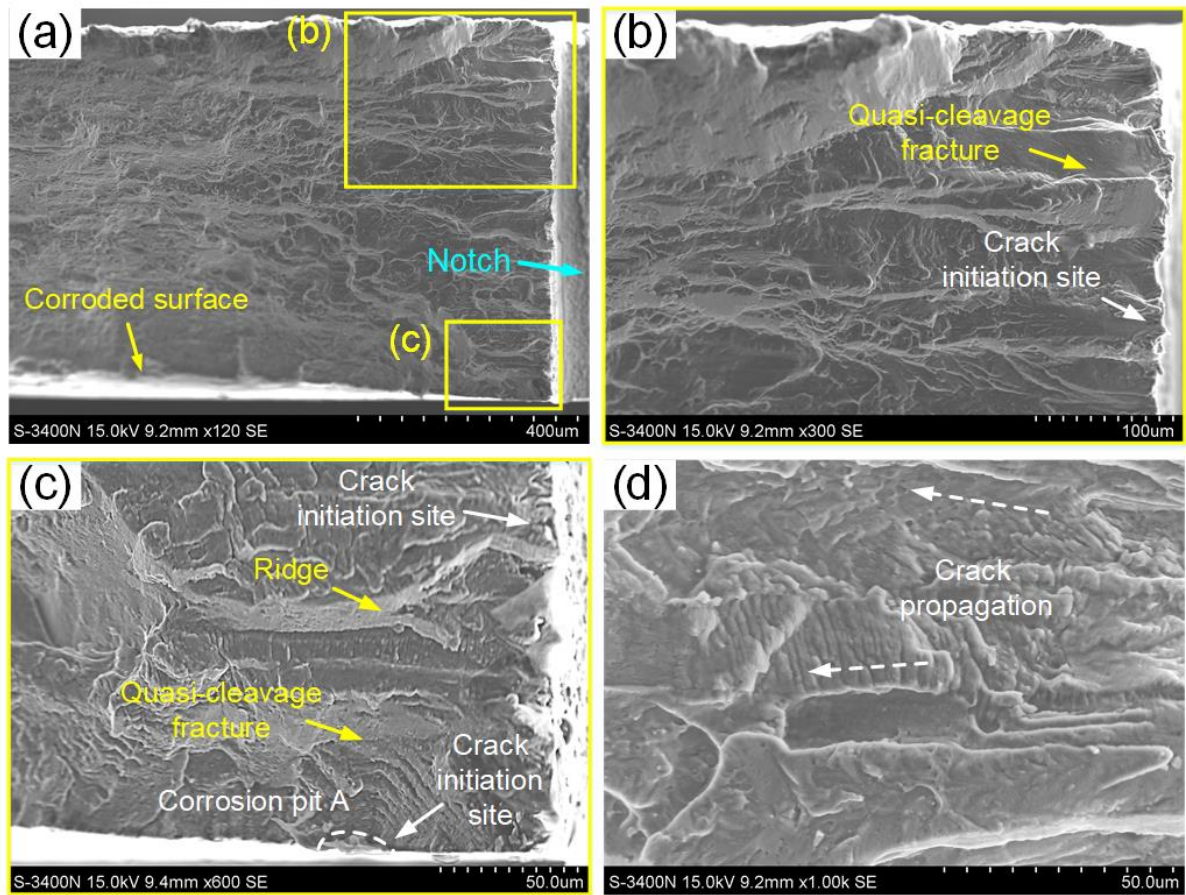


Fig. 8. Fracture morphology of specimen with a corrosion time of 0.5 hour, at a stress level of  $\sigma_{\max} = 333$  MPa, corresponding to the specimen shown in Fig. 4; the yellow squares are the field of view of subsequent images.



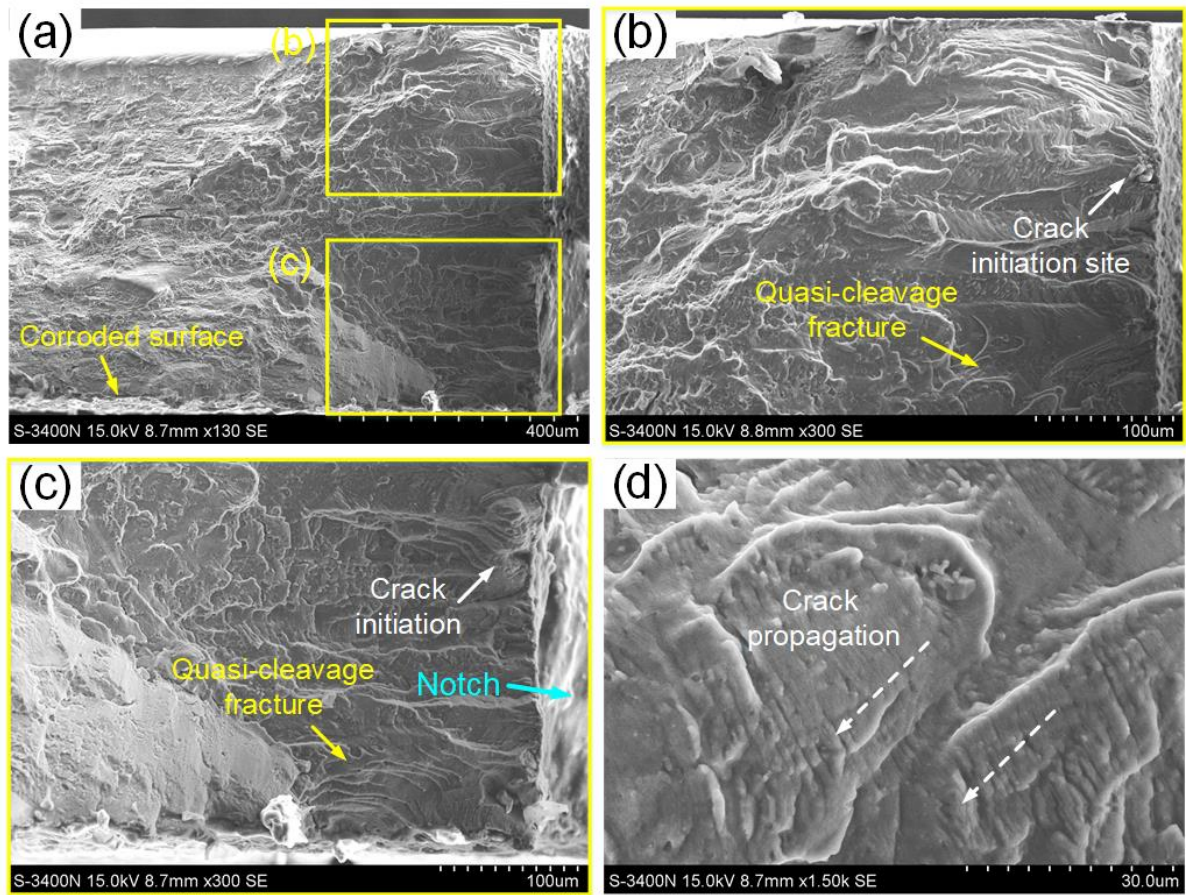


Fig. 9. Fracture morphology of specimen with a corrosion time of 0.5 hour, at a stress level of  $\sigma_{\max} = 389$  MPa, corresponding to the specimen shown in Fig. 5; the yellow squares are the field of view of subsequent images.

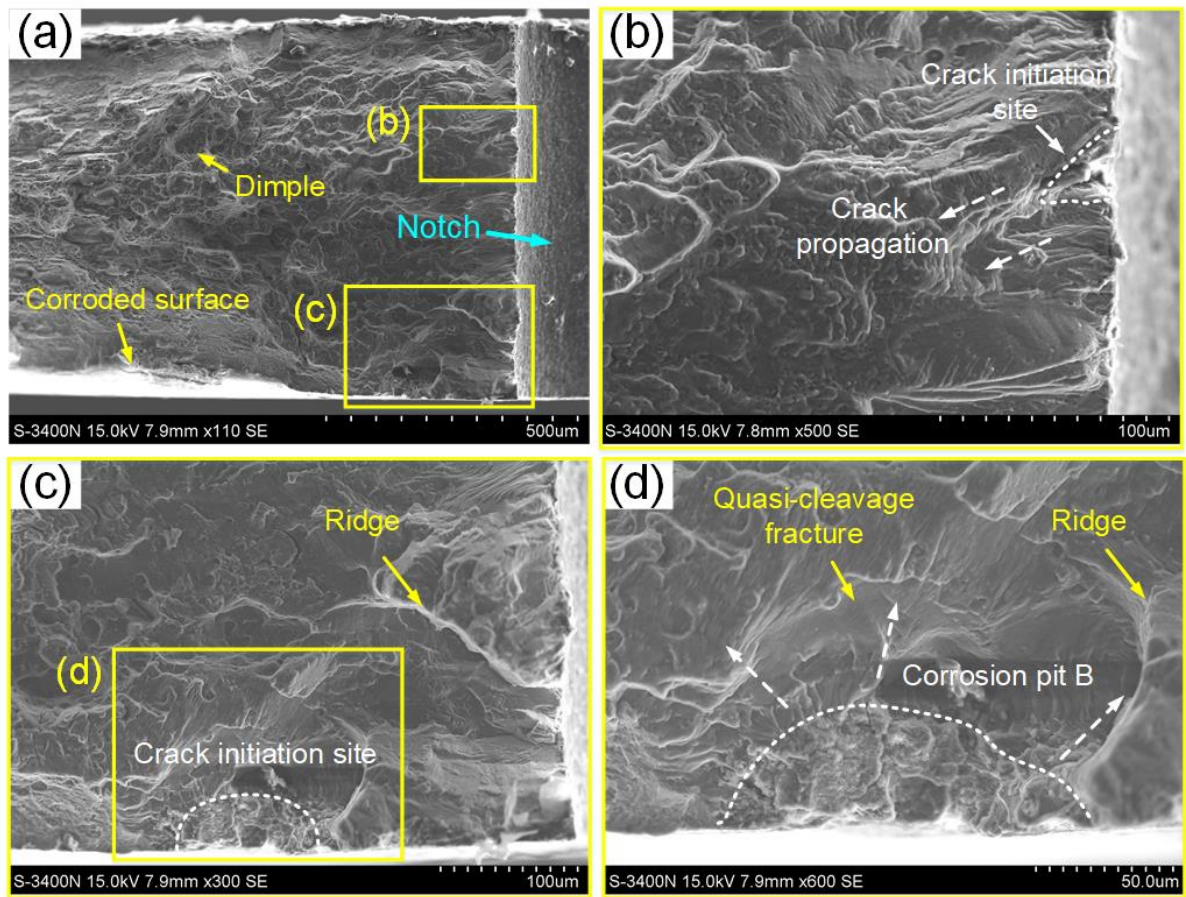


Fig. 10. Fracture morphology of specimen with a corrosion time of 1 hour, at a stress level of  $\sigma_{\max} = 333$  MPa, corresponding to the specimen shown in Fig. 6; the yellow squares are the field of view of subsequent images.



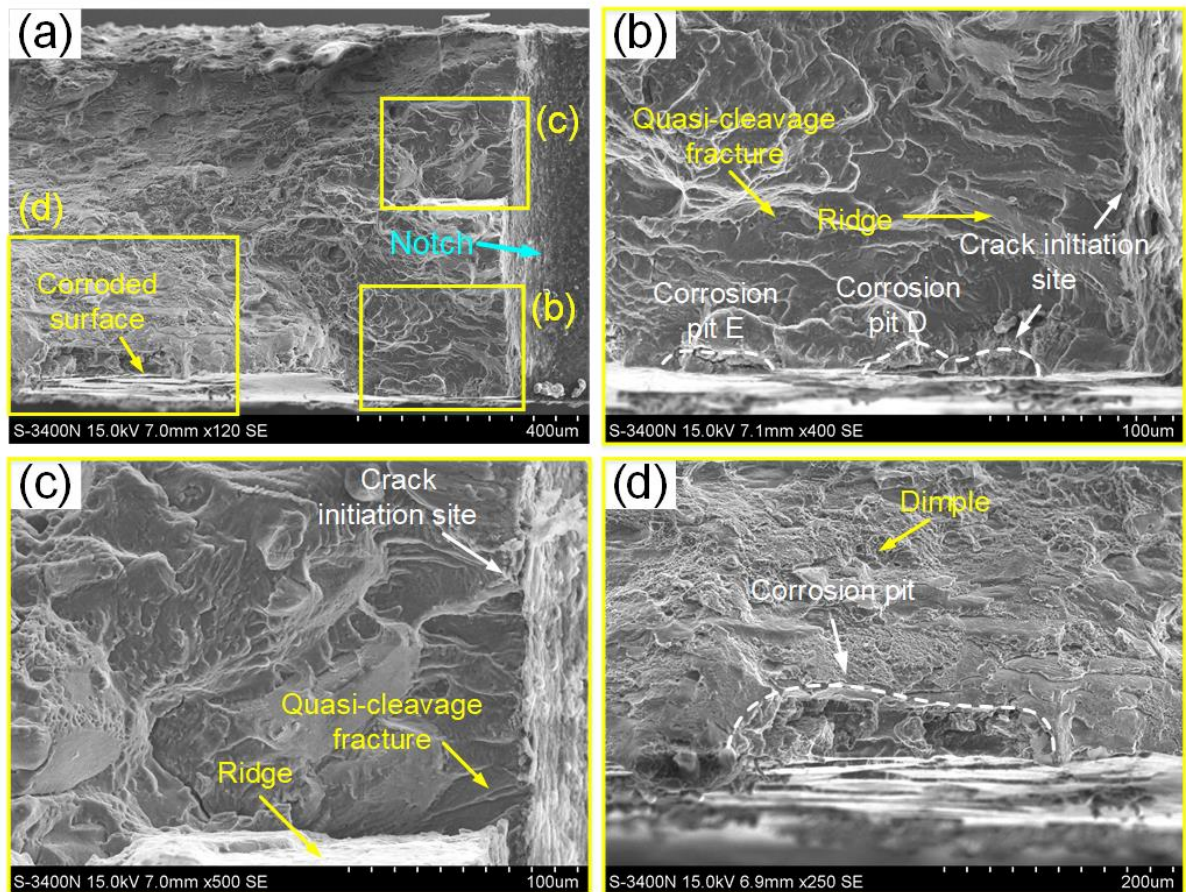


Fig. 11. Fracture morphology of specimen with a corrosion time of 1 hour, at a stress level of  $\sigma_{\max} = 389$  MPa, corresponding to the specimen shown in Fig. 7; the yellow squares are the field of view of subsequent images.

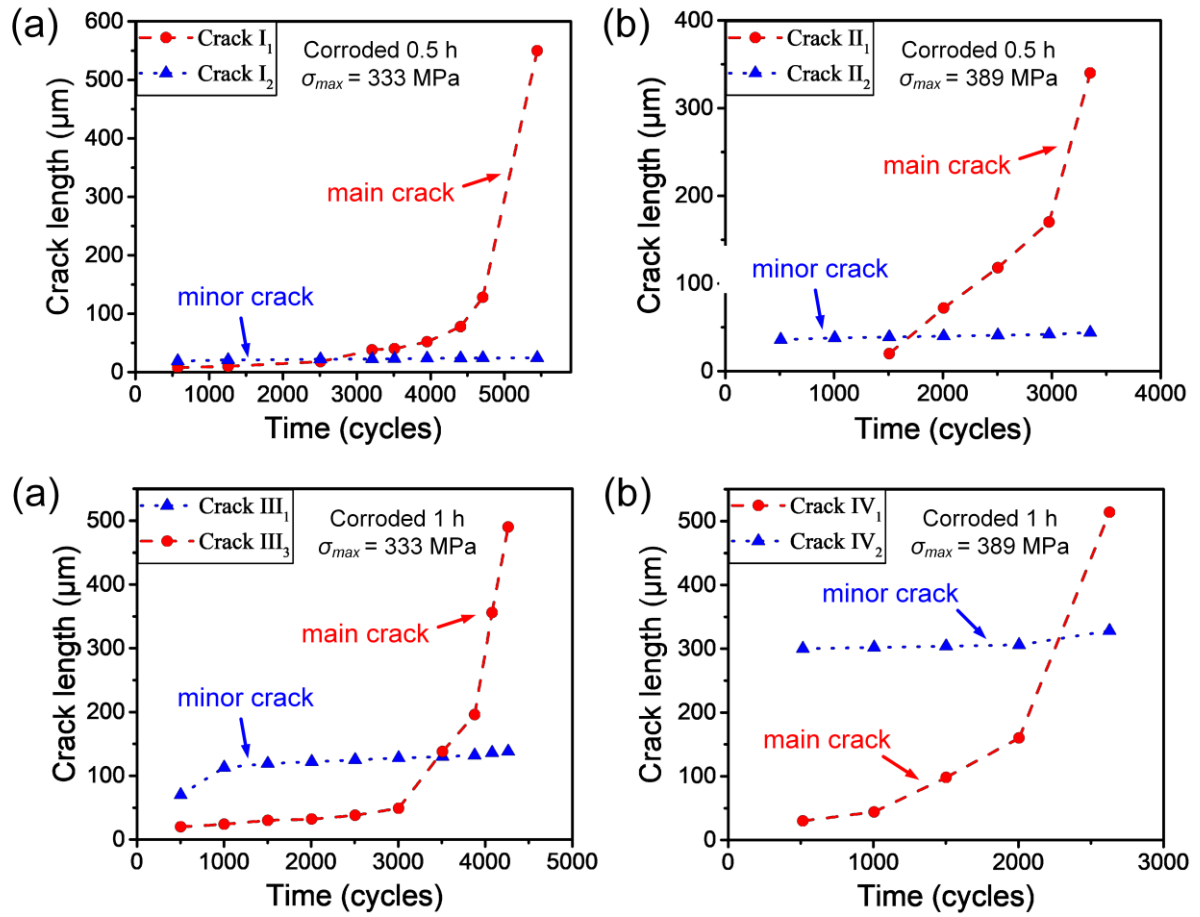


Fig. 12. Fatigue crack length curves of main crack (denoted by red line) and minor crack (denoted by blue line) versus fatigue cycle for different experimental conditions.